DOI: 10.1002/((please add manuscript number))
Article type: Communication

Exceptional performance of hierarchical Ni-Fe (hydr)oxide@NiCu electrocatalysts for water splitting

*Yongfang Zhou†, Zixu Wang†, Ziyan Pan, Le Liu, Jingyu Xi, and Xuanli Luo, and Yi Shen**

Prof. Dr. Y. Shen Mr. Z. Wang, Miss Y. Zhou and Z. Pan
School of Food Science and Engineering, South China University of Technology, Guangzhou, 510640, China
E-mail: feyshen@scut.edu.cn

Prof. Dr. J. Xi and Prof. Dr. L Liu
Institute of Green Chemistry and Energy, Graduate School at Shenzhen, Tsinghua University, Shenzhen 518055, P. R. China.

Dr. X Luo
Advanced Materials Research Group, Faculty of Engineering, University of Nottingham, Nottingham, NG7 2RD, UK

† These two authors contributed equally to this work

Keywords: water splitting, hydrogen evolution reaction, oxygen evolution reaction, layered double hydroxides and porous Ni-Fe oxides

The ever-increasing consumption of fossil fuels and resultant environmental issues, such as global warming, ozone layer depletion and acid rains, necessitate searching for clean energy sources.[1] Hydrogen is considered to be a promising alternative to fossil fuels by virtue of its high energy density and environmental-friendliness.[2] Renewable energy (such as electricity produced from photovoltaics and wind farms) powered water splitting provides an attractive method for sustainable production of hydrogen.[3] However, the two half electrochemical reactions involved in a water splitting process, namely, the oxygen evolution reaction (OER) and hydrogen evolution reaction (HER), are kinetically sluggish, leading to significant electrode overpotentials, and thus requires efficient electrocatalysts to improve energy efficiency.[3] Currently, precious-metal based electrocatalysts, such as Ir/Ru for OER and Pt for HER, could realize low overpotentials for water splitting. Unfortunately, the scarcity and high cost of these precious metals greatly prohibit their widespread applications. To this end, efforts have been devoted to searching for low-cost alternatives[4-8] and numerous transition-metal (hydr)oxides,[9-13] sulfides,[14-17] carbides,[18-20] phosphides[21-23] and even carbon-based materials[24-26] have so far been studied for HER/OER. In particular, the (hydr)oxides of nickel,[27-29] iron,[30-32] cobalt[33-35] and copper[36] have been reported as efficient HER and/or OER electrocatalysts. For instance, Gong *et al.* fabricated an electrolyzer using a nickel oxide/nickel supported by carbon nanotubes and Ni-Fe layered double hydroxide (LDH) as HER and OER electrocatalysts, respectively.[37] The resulting electrolyzer yielded a current density of 20 mA cm^{-2} at a voltage of 1.5 V. In addition, Luo *et al.* constructed a perovskite solar cell powered an electrolyzer using a bifunctional Ni-Fe LDH electrocatalyst for both OER and HER in alkaline electrolyte.[38] They obtained a solar-to-hydrogen efficiency of 12.3% at a photocurrent density of 10 mA cm^{-2} from the apparatus.

For the practical applications, integrating cathodic and anodic electrodes in an electrolyzer with the same electrolyte is highly beneficial for increasing energy efficiency and reducing fabrication cost.[39] Unfortunately, it is always challenging to couple HER and OER in the same electrolyte due to the incompatibility of the catalyst stability and activity. Recently, developing bifunctional electrocatalysts which possess high activity for both HER and OER has proved to be a promising route for overall water splitting.[40-45] For instance, Jia *et al.* assembled single layered NiFe LDH nanosheets on defective graphene. The resulting bifunctional catalyst yielded a current density of 20 mA cm^{-2} at a voltage of 1.5 V, which represents the highest activity for overall water splitting to date.41 Luo *et al.* synthesized a bifunctional electrocatalyst, consisting of Cu nanowires shelled with NiFe LDH nanosheets. It produced current densities of 10 and 100 mA cm^{-2} at potentials of 1.54 and 1.69 V, respectively.[42]

Despite numerous efforts devoted to exploring earth-abundant transition metal-based catalysts, high-performance bifunctional HER/OER electrocatalysts are still scarce. Critical issues related with transition metal (hydr)oxide electrocatalysts lie in the limited number of active sites and poor conductivity, leading to unsatisfactory performance for water splitting.[27] Note that the activity of metal (hydr)oxides could be greatly enhanced by delicately engineering their nanostructures. Herein, using earth-abundant transitional metal elements including nickel, iron and copper, the authors constructed three-dimensional core-shelled architectures, consisting of NiFe-LDH nanosheets/porous NiFe oxides assembled to metallic NiCu alloy, as bifunctional electrocatalysts for overall water splitting. The focus of this study is to optimize the activity of the catalysts by engineering their nanostructures. The prominent structural feature of the as-prepared catalysts lies in the presence of abundant heterogeneous nano-interfaces, endowing with not only the merits of the individual constituents, but also their synergistic effects in HER and OER processes. In addition, the assembly of ultrathin NiFe-LDH nanosheets or porous NiFe oxides onto the metallic NiCu could afford large surface areas, fast electron transfer, facile access to electrolyte and release of gas bubbles. Benefiting such structural merits, the as-prepared materials show excellent activity for both OER and HER. The outstanding performance for water splitting was demonstrated by a 1.5 V solar-panel powered electrolyzer, yielding current densities of 10 and 50 mA cm^{-2} at overpotentials of 293 and 506 mV, respectively.

The synthesis protocol starts from the NiCu nanoparticles which were synthesized via a polyol-assisted reduction process (see the details in the experimental section). The resulting NiCu nanoparticles have diameters of ca. 21±4 nm (see **Fig. S1**). XRD pattern of the NiCu nanoparticles (see **Fig. S2**) shows one set of diffraction peaks, which can be well indexed by JCPDS #04-0850, indicating the formation of NiCu alloy. Using the NiCu nanoparticles as seeds, NiFe-LDH@NiCu was obtained via self-assembly of NiFe-LDH nanosheets. The morphological structures of the as-prepared NiFe-LDH@NiCu were studied by field emission scanning electron microscopy (FESEM) and transmission electron microscopy (TEM) as shown in **Fig. 1**. FESEM images (see **Fig. 1a-c**) reveals that the resulting NiFe-LDH@NiCu possesses a three-dimensional hierarchical structure, consisting of numerous nanosheets self-assembled into quasi-spheres with diameters of 400-600 nm. TEM images (see **Fig. 1d, e**) show clear contrast between the center and periphery of the NiFe-LDH@NiCu nanoparticles, manifesting the formation of core-shell structure. The formation of such a core-shell structure is related to the synthesis protocol, which involves seed (NiCu nanoparticles) mediated growth of NiFe-LDH. High-resolution TEM image (see **Fig. 1f**) shows a bi-layered nanosheet with a thickness of ca. 1.6 nm. The average thickness between layers is estimated to be 0.8 nm, which is well matched with the spacing value of NiFe-LDH (003) planes. High-angle annular dark field scanning TEM (HAAD-STEM) image (see **Fig. 1g**) and corresponding electron energy loss spectroscopy (EELS) images (see **Fig. 1h-k**) vividly resolve the distribution of Fe, Cu, Ni and O elements. Notably, no other elements were detected from the sample, indicating its high purity. The crystallographic structure of the as-prepared NiFe-LDH@NiCu was examined by XRD. The diffraction peaks in the XRD profile can be well ascribed to cubic NiCu alloy phase (JCPDS #04-0850) and α-phase $Ni(OH)_2$ (JCPDS #038-0715 which is the same as NiFe-LDH) as shown in **Fig. S3**. Compared with β-phase NiFe-LDH, α-phase NiFe-LDH is a more active OER electrocatalyst.[33]

NiFe-LDH@NiCu was transformed into $NiFeO_x$@NiCu by a simple thermal treatment. **Fig. 2** shows the morphological structures of the resulting $NiFeO_x$@NiCu. Interestingly, the $NiFeO_x$@NiCu shows different morphology compared with the NiFe-LDH@NiCu sample. FESEM images (see Fig. **2a-c**) show that the NiFeOx@NiCu exhibit a well-defined spherical structure. TEM image (see Fig. **2d**) further indicates that the surface of the $NiFeO_x$@NiCu nanospheres are relatively smooth. HRTEM image (see Fig. **2e**) shows distinct lattice fringes with spacing values of 0.2 and 0.24 nm, corresponding to the inter-distance of $NiFeO_x$ (021) and (101) planes, respectively. HAAD-STEM image (see **Fig. 2f**) clearly reveals a porous structure of the $NiFeO_x$@NiCu nanosphere. The formation of porous structure could be attributed to the dehydration process at high temperatures. The distribution of Ni, Fe, Cu and O elements is also studied by HAAD-STEM (see **Fig. 2g**) and EELS mapping images (see **Fig. 2h-k**). The XRD pattern of the $NiFeO_x$@NiCu sample is shown in **Fig. S4**. The diffraction peaks can be well assigned to NiCu alloy phase (JCPDS #04-0850) and $NiFeO_x$ phase (JCPDS #44-1159). For comparison, NiFe-LDH sample was also synthesized. Shown in **Fig. S5**, the morphology of the NiFe-LDH sample is similar to that of NiFe-LDH@NiCu, consisting of ultrathin nanosheets self-assembled into large aggregates. Herein, it should be pointed out that the formation mechanism of the two materials are different. The formation of the NiFe-LDH@NiCu nanoarchitectures is attributed to the seed mediated growth process. In contrast, the hierarchical structure of the NiFe-LDH is related to the self-assembly process, in which ultrathin NiFe-LDH nanosheets are spontaneously aggregated to reduce the total surface energy. The morphology of the NiFe-LDH is further examined by atomic force microscopy as shown in **Fig. S6**. It indicates that the NiFe-LDH sample consists of numerous nanosheets aggreates, which is consistent with the TEM observation. The thickness of the NiFe-LDH was estimated to 2.4 nm, corresponding to a tri-layered nanosheet. XRD analyses indicate that the resulting NiFe-LDH possesses an identical phase structure of α-$Ni(OH)_2$ (JCPDS 038-0715) as shown in **Fig. S7**. The composition of the samples was analyzed by inductively coupled plasma atomic emission spectrometry (ICP-AES) as listed in **Table S1**. It should be pointed out that the content of oxygen in the sample was estimated by subtracting the total mass of the sample with those of metals, and that the results were carefully checked for reproducibility.

To analyze the electronic structures of the samples, X-ray photoelectron spectroscopy (XPS) tests were conducted. **Fig. S8a, b** and **c** show the Ni 2p, Fe 2p and Cu 2p core level spectra of the samples, respectively. All the spectra were corrected using the C 1s signal located at 284.5 eV and then carefully fitted using the software XPSPeak41. To decompose the XPS spectra, the constraints of equal spin–orbit splitting for the peaks in binding energy, peak area and full width at half maximum were thoroughly considered. The spectra consist of doublets of 3/2 and 1/2, and each doublet contains a major peak and a satellite peak. An inspection on the spectra could reveal distinct shifts in the binding energy (BE) of the elements. For instance, for Ni 2p 3/2, the NiCu sample exhibits a BE value of 854.2 eV. Such a BE value is higher than that of metallic nickel (852.9 eV), which could probably be attributed to the surface oxidation of the NiCu nanoparticles. The BE value of the NiFe-LDH and NiFe-LDH@NiCu (855.6 eV) is slightly lower than that of pure $Ni(OH)_2$ (856.0 eV), which could be related to the electron transfer arisen from the introduction of Fe in the sample. The $NiFeO_x$@NiCu has a BE value of 855.1 eV, which is a typical value of Ni^{2+} in the oxide state.[46] For Fe 2p 3/2, the NiFe-LDH has a BE value of 711.6 eV, which is larger than those of $NiFeO_x$@NiCu (710.2 eV) and NiFe-LDH@NiCu (710.1 eV). More interestingly, the profiles of the Fe 2p spectra of the three samples are quite different. For Cu 2p 3/2, the BE value of NiCu (932.4 eV) is lower than those of $NiFeO_x$@NiCu (933.3 eV) and NiFe-LDH@NiCu (933.9 eV). The XPS results suggest that the electronic structures of the elements are different in the samples owing to the coupling interaction. The surface composition of the catalysts was also analyzed by XPS as shown in **Table S2**. The surface of NiCu nanoparticles consist of 28.9% oxygen due to the surface oxidation. The surface Ni/Cu ratio is estimated to be 2.76, which is lower than the bulky Ni/Cu ratio (3.01) as determined by ICP-AES, indicating the surface segregation of copper in the sample. In the NiFe-LDH sample, the surface Ni/Fe ratio is determined to be 3.875, which is large than the bulky Ni/Fe ratio (3.185). It is noteworthy that the contents of copper in the surfaces of the $NiFeO_x$@NiCu and NiFe-LDH@NiCu samples are considerably lower than the bulky Cu contents, which could be explained from their core-shell structure.

The OER activity of the as-prepared catalysts was characterized in O_2-saturated 1.0 M KOH solution and benchmarked against that of a commercial RuO_2 catalyst. **Fig. 3a** shows the polarization curves of the catalysts recorded at a scan rate of 5 mV s^{-1}. The RuO_2, NiCu, NiFe-LDH, NiFe-LDH@NiCu and NiFeOx@NiCu exhibited onset potentials of 30, 121, 144, 96 and 76 mV, respectively. Among the five catalysts, the NiFe-LDH@NiCu exhibits the highest geometric current densities. For clarity, **Fig. 3b** comparatively shows the overpotentials of the catalysts at current densities of 10 and 20 mA cm^{-2}. To gain a geometric current density (*j*) of 10 mA cm^{-2}, the NiFe-LDH@NiCu requires an overpotentials of 218 mV, which is smaller than those of 249, 265, 316 and 327 eV for the RuO_2, NiFe-LDH, $NiFeO_x$@NiCu and NiCu samples, respectively. Such an overpotential is only slightly higher than those of the Cu@NiFe-LDH (199 mV)[42] and NiFe-LDH-NS@DG (210 mV),[41] but smaller than those of other LDH-based catalysts reported in the literature as shown in **Table S3**, rendering the resulting NiFe-LDH@NiCu as one of the best OER electrocatalysts. Interestingly, at a current density of 20 mA cm^{-2}, the overpotential of the NiFe-LDH catalyst (300 mV) is smaller than that of the RuO_2 (307 eV), manifesting that the NiFe-LDH outperforms the RuO_2 at high current densities, which can be evidenced from the polarization curves shown in **Fig. 3a**. To further compare the activity, the current densities of the catalysts at an overpotential of 320 mV are shown in **Fig. S9**. It shows that the current densities of the catalysts follow the sequence of NiFe-LDH@NiCu (44.9 mA cm^{-2}) > NiFe-LDH (28.5 mA cm^{-2}) > RuO_2 (23.5 mA cm^{-2}) > $NiFeO_x$@NiCu (10.5 mA cm^{-2}) > NiCu (9.0 mA cm^{-2}). For better comparison, the mass-normalized current densities of the catalysts are calculated as shown in **Fig. S10**. It shows that among the five catalysts, the NiFe-LDH@NiCu also possesses the highest mass-normalized current density. Specifically, at an overpotential of 300 mV, the NiFe-LDH@NiCu catalyst has a mass-normalized current density of 429.1 A g^{-1}, which is 4.72, 4.29, 1.85 and 1.74 times those of the NiCu, $NiFeO_x$@NiCu, RuO_2 and NiFe-LDH, respectively. Such a remarkable mass-normalized current density of the NiFe-LDH@NiCu is also larger than those of γ-CoOOH (66.6 A g^{-1}),[47] NiFeMo alloy (113 A g^{-1}),[39] $Ni_{0.8}Fe_{0.2}O_xH_y$ film (140 A g^{-1}),[48] CoMn LDH (159 A g^{-1})[33] and NiFe-LDH nanoparticles (200 A g^{-1} at an overpotential of 260 mV)[49] reported in the literature. To study the intrinsic activity, turnover frequencies (TOFs) of the catalysts were calculated by assuming that nickel is considered as the active sites in the catalysts. As shown in **Fig. 3c**, the TOF values of the catalysts follow the order of RuO_2 > NiFe-LDH@NiCu > NiFe-LDH >

$NiFeO_x$@NiCu > NiCu at overpotentials less than 0.35 V. When the overpotentials are over 0.35 V, the order changes into NiFe-LDH > RuO_2 > NiFe-LDH@NiCu > $NiFeO_x$@NiCu > NiCu. Specifically, at an overpotential of 350 mV, the NiFe-LDH@NiCu possesses a TOF value of 0.341 s^{-1}, which is slightly smaller than those of RuO_2 (0.344 s^{-1}) and NiFe-LDH (0.344 s^{-1}), but larger than those of NiCu (0.034 s^{-1}) and $NiFeO_x$@NiCu (0.064 s^{-1}). Such a TOF value of the NiFe-LDH@NiCu is only next to that of NiFe LDH/CNT (0.56 s^{-1}),[30] but much larger than those of exfoliated NiCo LDH (0.011 s^{-1}),[50] CoMn LDH (0.075 s^{-1})[33] and $NiFeO_x$ (0.21 s^{-1})[12] reported in the literature. **Fig. 3d** shows the Tafel plots of the catalysts. The NiFe-LDH possesses a Tafel slope of 53.0 mV dec^{-1}, which is close to that of the NiFe-LDH@NiCu (56.9 mV dec^{-1}) and much smaller than those of RuO_2 (100.3 mV dec^{-1}), $NiFeO_x$@NiCu (157.2 mV dec^{-1}) and NiCu (218.6 mV dec^{-1}), indicating the faster OER kinetics. The durability of the catalysts was evaluated by chronopotentiometry tests at a current density of 10 mA cm^{-2} as shown in **Fig. S11**. Overall, the overpotentials of the catalysts show slight increases during the testing time, suggesting that the catalysts exhibit good stability for the OER process. The durability of the NiFe-LDH@NiCu catalyst was further characterized by chronoamperometric measurements as shown in **Fig. 3e**. At overpotentials of 250 and 300 mV, the current densities are quite stable, further verifying the excellent durability of the NiFe-LDH@NiCu catalyst. The morphology of the spent NiFe-LDH@NiCu after the chronoamperometric tests was observed by FESEM. Shown in **Fig. S12a, b**, the spent NiFe-LDH@NiCu well preserves the 3D hierarchical structure. The XRD profiles of the pristine and spent NiFe-LDH@NiCu samples also showed negiliable variations as evidence from **Fig. S12c**.

To explore the origin of the superior activity of the NiFe-LDH@NiCu catalyst, the double-layer capacitance (C_{dl}) of the catalyst, which is well correlated with its electrochemical active surface area (ECSA),[33] was determined by cyclic voltammetry (CV) measurements. **Fig. S13** shows the CV curves recorded in the potentials ranging from 0.4 to

0.6 V and the corresponding capacitive currents $(j_a\text{-}j_c)/2$ as a function of scan rate. The capacitive currents possess a linear relationship with scan rate and the slope of the curve correspond to the C_{dl} of the catalyst. The NiFe-LDH@NiCu possesses a C_{dl} value of 1.78 mF cm^{-2}, which is larger than those of NiCu (0.31 mF cm^{-2}), NiFeO$_x$@NiCu (1.24 mF cm^{-2}) and RuO$_2$ (0.37 mF cm^{-2}), but smaller than that of NiFe-LDH (2.16 mF cm-^{2}), suggesting that the ECSA is not the only reason for the superior activity of the NiFe-LDH@NiCu. To gain deep insight into the activity of the NiFe-LDH@NiCu, electrochemical impedance spectroscopy (ESI) tests were performed. The resulting Nyquist plots are shown in **Fig. 3f**. The values of charge-transfer resistance (R_{ct}) of the catalysts are determined to be 7.3, 7.5, 17.4, 22.6 and 48.6 Ω for the NiFe-LDH@NiCu, RuO$_2$, NiFe-LDH, NiFeO$_x$@NiCu and NiCu catalysts, respectively. The smallest R_{ct} values of the NiFe-LDH@NiCu catalyst suggests the fastest OER kinetics, which could be attributed to the synergistic effects of NiFe-LDH shell and metallic NiCu core. Importantly, the Nyquist plot of the spent NiFe-LDH@NiCu catalyst after the chronoamperometric measurements show negligible variations as shown in **Fig. S14**, manifesting the excellent OER durability of the catalysts.

Apart from the OER performance, the HER performance of the catalysts was also evaluated. For comparison, the activity of the catalysts was benchmarked against a precious Pt catalyst. Shown in **Fig. 4a**, the HER activity of the catalysts follows the sequence of Pt plate > NiFeO$_x$@NiCu > NiCu > NiFe-LDH@NiCu > NiFe-LDH. The onset potentials of the Pt, NiCu, NiFe-LDH, NiFe-LDH@NiCu and NiFeOx@NiCu were determined to be 3, 21, 49, 16 and 11 mV, respectively. To achieve a geometric current density of 10 mA cm^{-2}, the NiFeO$_x$@NiCu catalyst requires an overpotential of 66 mV, which is slightly higher than that of Pt plate (53 mV) and lower than those of NiCu (95 mV), NiFe-LDH@NiCu (112 mV) and NiFe-LDH (245 mV) as shown in **Fig. S15**. To the best of the authors' knowledge, such a low overpotential of the NiFeO$_x$@NiCu is a record for the transitional metal (hydr)oxide-based HER catalysts as shown in **Table S4**. **Fig. 4b** shows the Tafel plots of the catalysts. The

$NiFeO_x$@NiCu possess a Tafel slope of 67.8 mV dec^{-1}, which is slightly larger than that of Pt plate (44.2 mV dec^{-1}), but much less than those of NiCu (136.2 mV dec^{-1}), NiFe-LDH@NiCu (168.2 mV dec^{-1}) and NiFe-LDH (194.2 mV dec^{-1}), indicating the faster reaction kinetics. The HER stability of the catalysts was characterized by chronoamperometric measurements at an applied potential of 100 mV as shown in **Fig. S16**. It shows that the current densities only slightly decrease in the initial periods of testing time (ca. 100 min) and then remain constant with increasing time, suggesting the good HER durability of the catalysts. The chronoamperometric curves of the $NiFeO_x$@NiCu recorded at applied potentials of 100 and 150 mV are comparatively shown in **Fig. 4c**. At an overpotential of 150 mV, the $NiFeO_x$@NiCu exhibits a stable current density of 49.3 mA cm^{-2}, which is much higher than that of 23.9 mA cm^{-2} at an overpotential of 100 mV. These chronoamperometric results are consistent with the polarization curves shown in **Fig. 4a**. After the chronoamperometric tests, the morphology the spent $NiFeO_x$@NiCu was also observed by FESEM as shown in **Fig. S17a, b**. It indicates that the spherical structure is well maintained after the long-term HER tests. The diffraction peaks of the spent samples can be also matched with those of the pristine samples.

To reveal the HER kinetics of the catalysts, ESI measurements were conducted at an overpotential of 150 mV. The Nyquist plots in **Fig. 4d** reveals that the $NiFeO_x$@NiCu exhibits an ohmic resistance (R_c) of 0.42 Ω, which is larger than those of Pt plate (0.08 Ω) and NiCu (0.36 Ω), but smaller than those of NiFe-LDH@NiCu (0.89 Ω) and NiFe-LDH (1.21 Ω), manifesting that the presence metallic NiCu in the catalysts enhances the conductivity. In addition, the $NiFeO_x$@NiCu has a R_{ct} value of 7.2 Ω, which is larger than that of Pt plate (5.1 Ω), but smaller than those of NiCu (7.3 Ω), NiFe-LDH@NiCu (25.3 Ω) and NiFe-LDH (29.6 Ω), suggesting the facile charge transfer in the $NiFeO_x$@NiCu catalyst. After the chronoamperometric tests, the R_c and R_{ct} values of the spent $NiFeO_x$@NiCu catalyst increase as shown in **Fig. S18**. This could be probably attributed to the isolation of catalyst nanoparticles from the electrode due to the bubbling of hydrogen gas.

The results suggest that the NiFe-LDH@NiCu exhibits the best OER activity while the $NiFeO_x$@NiCu shows the superior HER activity. Inspired by their outstanding performance, the authors employed these two electrocatalysts to construct an electrolyzer for water splitting. For comparison, the reference anodic catalyst, *i.e.*, RuO_2 and the reference cathodic catalyst *i.e.*, Pt/C were also used and the performance of four catalyst pairs including (I) RuO_2(+)||$NiFeO_x$@NiCu(-), (II) RuO_2(+)||Pt(-), (III) NiFe-LDH@NiCu(+)||Pt(-), and (IV) NiFe-LDH@NiCu(+)||NiFeOx@NiCu(-) were evaluated. For the overall water splitting, the catalyst pairs of (I), (II), (III) and (IV) had onset potentials of 63, 52, 129 and 117 mV, respectively. Shown in **Fig. 5a**, the combination (III) outperforms the three another catalyst pairs at potentials less than 1.67 V. When the potential is over 1.67 V, the combination (IV) possesses the highest current densities for water splitting. For clarity, **Fig. S19** shows the overpotentials of the catalyst combinations at current densities of 10 and 50 mA cm^{-2}. A current density of 10 mA cm^{-2} is obtained from the combinations (I), (II), (III) and (IV) at potentials of 1540, 1528, 1503 and 1523 mV, respectively. Such performance of these electrolyzers outperforms most of the electrolyzers reported in the literature as shown in **Table S5**. In particular, the electrolyzers constructed with the catalyst combinations (III) and (IV) have had the second-best performance to date, only next to the electrolyzer integrated with a NiFe-LDH-NS@DG electrocatalyst.[41] In contrast, to achieve a current density of 50 mA cm^{-2}, the potentials increase to 1976, 1853, 1782 and 1736 mV for the combinations (I), (II), (III) and (IV), respectively. Since large current densities are economically favorable for water splitting, the combination (III) is more feasible for the practical applications. To illustrate the performance of the catalysts, the authors utilized a solar panel to power the water splitting process as depict in **Fig. 5b**. When a 1.5 V solar panel is used, considerable hydrogen and oxygen bubbles are generated from the electrodes using the catalyst combinations of (II) (see **video II** in the Supporting Information), (III) (see **video III**) and (IV) (see **video IV**) are utilized. On the contrary, few gas bubbles are produced from the combination of (I) (see **video I**) owing to the slow reaction kinetics. When a 2.0 V solar panel was used, the generation of gas bubbles from the combination of (IV) becomes more intense (see **video V**). Interestingly, the generation of gas bubbles are closely related to the intensity of the sunlight, which is attributed to the variations of current densities arisen from voltage fluctuations.

In summary, three-dimensional core-shell structured NiFe-LDH@NiCu and $NiFeO_x$@NiCu architectures were synthesized as bifunctional electrocatalysts for overall water splitting. The as-prepared NiFe-LDH@NiCu catalyst shows superior OER performance, resulting in an overpotential of 218 mV at a current density of 10 mA cm^{-2}, which outperforms the precious RuO_2 catalyst. The resulting $NiFeO_x$@NiCu possesses outstanding HER activity, leading to an overpotential of 66 mV at a current density of 10 mA cm^{-2}, which is only slightly higher than that of precious Pt catalyst (53 mV). The excellent activity of the NiFe-LDH@NiCu and $NiFeO_x$@NiCu was demonstrated by a 1.5 V solar-panel powered electrolyzer, yielding current densities of 10 and 50 mA cm^{-2} at overpotentials of 293 and 506 eV, respectively, which renders the as-prepared material as the second best bifunctional electrocatalyst so far. Such remarkable performance of the NiFe-LDH@NiCu and $NiFeO_x$@NiCu was attributed to the unique structures with abundant heterogeneous nano-interfaces, which not only afford the merits of the components, but also facilitate their synergistic effects in HER/OER processes. In addition, the assembly of ultrathin NiFe-LDH nanosheets or porous NiFe oxides onto the metallic NiCu core could afford large surface areas, fast electron transfer, facile access to electrolyte and fast release of gas bubbles. This work could shed new insight on designing advanced electrocatalysts for water splitting.

Experimental Section

See the details in the Supporting information.

Supporting Information

Supporting Information is available from the Wiley Online Library or from the author.

Acknowledgements
The project was financially supported by the Scientific Research Foundation for the Returned Overseas Chinese Scholars, State Education Ministry, the Natural Science Foundation of Guangdong Province, China (2014A030310315), the Ministry of Science and Technology of China (Grant Nos. 2014CB932400 and 2017YFB0701604), the National Natural Science Foundation of China (Grant No. 51232005), and the Shenzhen Projects for Basic Research (Grant KQCX20140521161756227 and JCYJ20170307154206288). Luo acknowledged the support of a Daphne Jackson Trust fellowship and its sponsors: Royal Academy of Engineering and the University of Nottingham.

Received: ((will be filled in by the editorial staff))
Revised: ((will be filled in by the editorial staff))
Published online: ((will be filled in by the editorial staff))

[1] J. A. Turner, *Science* **2004**, *305*, 972

[2] Z. W. Seh, J. Kibsgaard, C. F. Dickens, I. Chorkendorff, J. K. Nørskov, T. F. Jaramillo, *Science* **2017**, *355*, 4998

[3] a) N. S. Lewis, D. G. Nocera, *Proc. Natl. Acad. Sci. U.S.A.* **2006**, *103*, 15729; b) Y. Jia, J. Chen, X. D. Yao, *Mater. Chem. Front.* 2018, *2*, 1250; c) L. Zhuang, Y. Jia, T. He, A. Du, X. Yan, L. Ge, Z. Zhu, X. D. Yao, *Nano Research* **2018**, *11*, 3509

[4] a) M. G. Walter, E. L. Warren, J. R. McKone, S. W. Boettcher, Q. X. Mi, E. A. Santori N. S. Lewis, *Chem. Rev.* **2010**, *110*, 6446; b) Y. G. Li, H. J. Dai, *Chem. Soc. Rev.* **2014**, *43*, 5257

[5] a) Y. Shen, A. C Lua, J. Xi, X. Qiu, *ACS Appl. Mater. Interfaces* **2016**, *8*, 3464; b) Y. Shen, Y. Zhou, D. Wang, X. Wu, J. Li, J. Xi, *Adv. Energy Mater.* **2018**, *8*, 1701759

[6] C. G. Morales-Guio, L. A. Stern, X. L. Hu, *Chem. Soc. Rev.* **2014**, *43*, 6555

[7] X. X. Zou, Y. Zhang, *Chem. Soc. Rev.* **2015**, *44*, 5148

[8] N. T. Suen, S. F. Hung, Q. Quan, N. Zhang, Y. J. Xu, H. M. Chen, *Chem. Soc. Rev.* **2017**, *46*, 337

[9] B. Weng, F. Xu, C. Wang, W. Meng, C. Grice, *Energy Environ. Sci.* **2017**, *10*, 121

[10] L. Qian, Z. Lu, T. Xu, X. Wu, Y. Yang, Y. Tian, Y. Li, Z. Huo, X. Sun, X. Duan, *Adv. Energy Mater.* **2015**, *5*, 1500245

[11] Y. Liang, Y. Li, H. Wang, J. Zhou, J. Wang, T. Regier, H. Dai, *Nat. Mater.* **2011**, *10*, 780

[12] L. Trotochaud, J. K. Ranney, K. N. Williams, S. W. Boettcher, *J. Am. Chem. Soc.* **2012**, *134*, 17253

[13] J. Suntivich, K. J. May, H. A. Gasteiger, J. B. Goodenough, Y. Shao-Horn, *Science* **2011**, *334*, 1383

[14] J. Kibsgaard, Z. Chen, B. N. Reinecke, T. F. Jaramillo, *Nat. Mater.* **2012**, *11*, 963

[15] M. S. Faber, R. Dziedzic, M. A. Lukowski, N. S. Kaiser, Q. Ding, S. Jin, *J. Am. Chem. Soc.* **2014**, *136*, 10053

[16] X. Y. Yu, L. Yu, H. B. Wu, X. W. D. Lou, *Angew. Chem.* **2015**, *127*, 5421.

[17] D. Y. Wang, M. Gong, H. L. Chou, C. J. Pan, H. A. Chen, Y. Wu, M. C. Lin, M. Guan, J. Yang, C. W. Chen, Y. L. Wang, B. J. Hwang, C. C. Chen, H. Dai, *J. Am. Chem. Soc.* **2015**, *137*, 1587

[18] a) Y. Shen, L. Li, J. Xi, X. Qiu, *J. Mater. Chem. A* 2016, *4*, 5817; b) Y. Shen, B. Gong, *J. Electrochem. Soc.* **2016**, *163*, H1060

[19] a) F. X. Ma, H. B. Wu, B. Y. Xia, C. Y. Xu, X. W. D. Lou, *Angew. Chem.* **2015**, *54*, 15615; b) Y. P. Liu, G. T. Yu, G. D. Li, Y. H. Sun, T. Asefa, W. Chen, X. *Angew. Chem.* **2015**, *127*, 10752

[20] X. Fan, H. Zhou, X. Guo, *ACS Nano* **2015**, *9*, 5125

[21] J. Li, M. Yan, X. Zhou, Z. Q. Huang, Z. Xia, C. R. Chang, Y. Ma, Y. Qu, *Adv. Funct. Mater.* **2016**, *26*, 6785−6796.

[22] Y. Tan, H. Wang, P. Liu, Y. Shen, C. Cheng, A. Hirata, T. Fujita, Z. Tang, M. Chen, *Energy Environ. Sci.* **2016**, *9*, 2257

[23] C. Du, L. Yang, F. Yang, G. Cheng, W. Luo, *ACS Catal.* **2017**, *7*, 4131

[24] Q. Han, B. Wang, Y. Zhao, C. Hu, L. Qu, *Angew. Chem.* **2015**, *54*, 11433

[25] J. Duan, S. Chen, M. Jaroniec, S. Z. Qiao, *ACS Nano* **2015**, *9*, 931

[26] Y. Zheng, Y. Jiao, L. H. Li, T. Xing, Y. Chen, M. Jaroniec, S. Z. Qiao, *ACS Nano* **2014**, *8*, 5290.

[27] V. Vij, S. Sultan, A. M. Harzandi, A. Meena, J. N. Tiwari, W. G. Lee, T. Yoon, K. S. Kim, *ACS Catal.* **2017**, *7*, 7196.

[28] H. Liang, F. Meng, M. C. Acevedo, L. Li, A. Forticaux, *Nano Lett.* **2015**, *15*, 1421

[29] M. Gao, W. Shen, Z. Zhuang, Q. Fang, S. Gu, J. Jiang, Y. Yan, *J. Am. Chem. Soc.* **2014**, *136*, 7077.

[30] M. Gong, Y. Li, H. Wang, Y. Liang, J. Z. Wu, J. Zhou, J. Wang, T. Regier, F. Wei, H. Dai, *J. Am. Chem. Soc.* **2013**, *135*, 8452

[31] L. Qian, Z. Lu, T. Xu, X. Wu, Y. Yang, Y. Tian, Y. Li, Z. Huo, X. Sun, X. Duan, *Adv. Energy Mater.* **2015**, *5*, 1500245

[32] C. Chen, T. Wang, J. Zhang, P. Liu, H. Sun, X. Zhuang, M. Chen, X. Feng, *Adv. Mater.* **2018**, *30*, 1706279

[33] F. Song, X. Hu, *J. Am. Chem. Soc.* **2014**, *136*, 16481

[34] Z. Zhao, H. Wu, H. He, X. Xu, Y. Jin, *Adv. Funct. Mater.* **2014**, *24*, 4698

[35] S. Mao, Z. H. Wen, T. Z. Huang, Y. Hou, J. H. Chen, *Energy Environ. Sci.* **2014**, *7*, 609

[36] M. Jahan, Z. Liu, K. P. A. Loh, *Adv. Funct. Mater.* **2013**, *23*, 5363

[37] M. Gong, W. Zhou, M. C. Tsai, J. Zhou, M. Guan, M. C. Lin, B. Zhang, Y. Hu, D. Y. Wang, J. Yang, S. J. Pennycook, B. J. Hwang, H. Dai, *Nat. Commun.* **2014**, *5*, 4695.

[38] J. Luo, J. H. Im, M. T. Mayer, M. Schreier, M. K. Nazeeruddin, N. G. Park, S. D. Tilley, H. J. Fan, M. Grätzel, *Science* **2014**, *345*, 1593

[39] F. Qin, Z. Zhao, M. K. Alam, Y. Ni, F. *ACS Energy Lett.* **2018**, *3*, 546

[40] A. Wang, H. Xu, G. R. Li, *ACS Energy Lett.* **2016**, *1*, 445−453.

[41] Y. Jia, L. Zhang, G. Gao, H. Chen, B. Wang, J. Zhou, M. T. Soo, M. Hong, X. Yan, G. Qian, J. Zou, A. Du, X. Yao, *Adv. Mater.* **2017**, *29*, 1700017

[42] L. Yu, H. Zhou, J. Sun, F. Qin, F. Yu, J. Bao, Y. Yu, S. Chen, Z. Ren, *Energy Environ. Sci.* **2017**, *10*, 1820

[43] M. Ledendecker, S. K. Calderon, C. Papp, H. P. Steinruck, M. Antonietti, M. Shalom, *Angew. Chem.* **2015**, *127*, 12538.

[44] L. Feng, F. Song, X. Hu. *Energy Environ. Sci.* **2015**, *8*, 2347.

[45] C. Tang, R. Zhang, W. Lu, L. He, X. Jiang, A. M. Asiri, X. Sun, *Adv. Mater.* **2017**, *29*, 1602441

[46] T. Yoshida, K. Yamasaki, *Bull. Chem. Soc. Jpn.* **1981**, *54*, 935

[47] J. Huang, J. Chen, T. Yao, J. He, S. Jiang, Z. Sun, Q. Liu, W. Cheng, F. Hu, Y. Jiang, Z. Pan, S. Wei, *Angew. Chem. Int. Ed.* **2015**, *54*, 8722.

[48] M. B. Stevens, L. J. Enman, A. S. Batchellor, M. R. Cosby, A. E. Vise, C. D. M. Trang, S. W. Boettcher, *Chem. Mater.* **2017**, *29*, 120.

[49] R. Chen, G. Sun, C. Yang, L. Zhang, J. Miao, H. Tao, H. Yang, J. Chen, P. Chen, B. Liu, *Nanoscale Horiz.* **2016**, *1*, 156.

[50] F. Song, X. L. Hu, *Nat. Commun.* **2014**, *5*, 4477

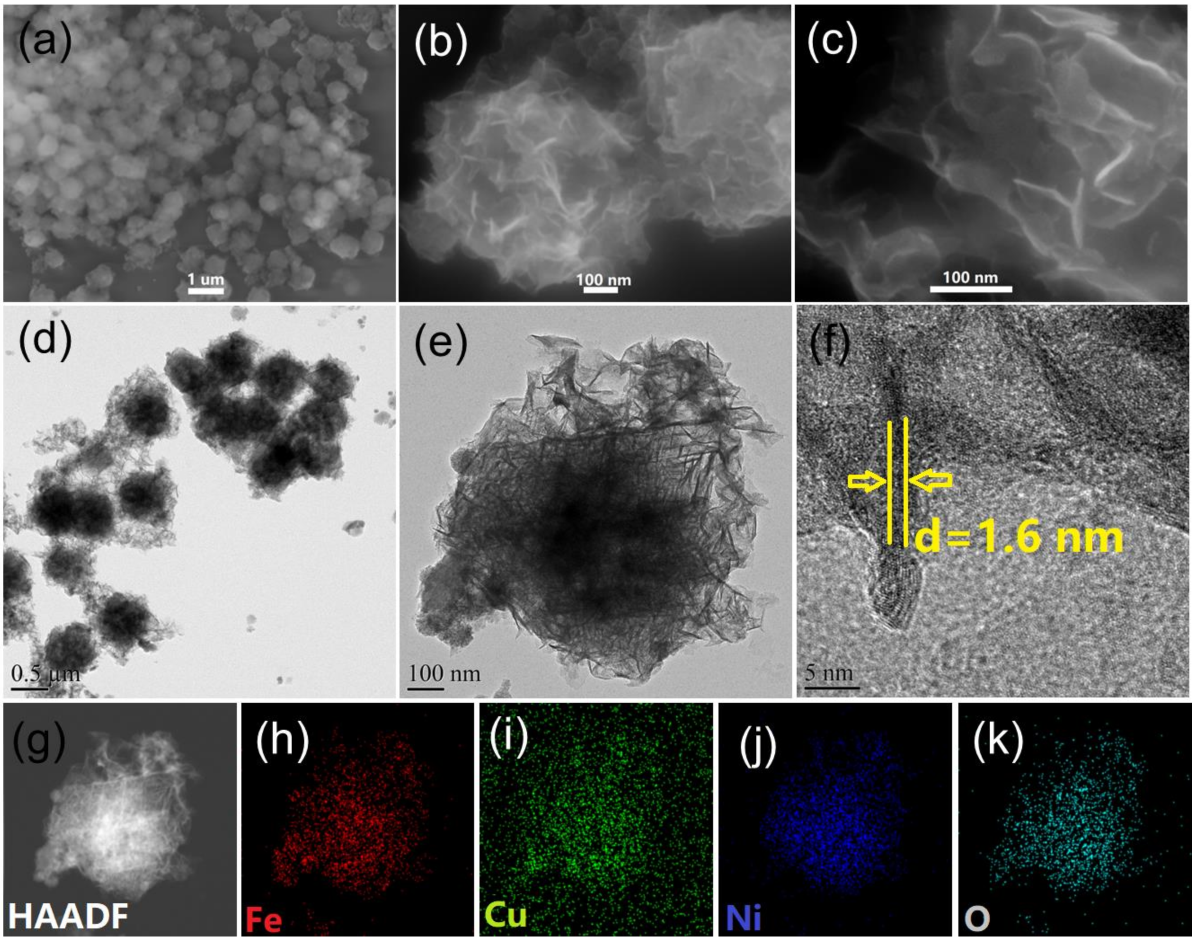

Fig. 1 (a-c) FESEM, (d-f) TEM, (g) HAADF-STEM images of NiFe-LDH@NiCu, and corresponding EELS mapping of (h) iron, (i) copper, (j) nickel and (k) oxygen.

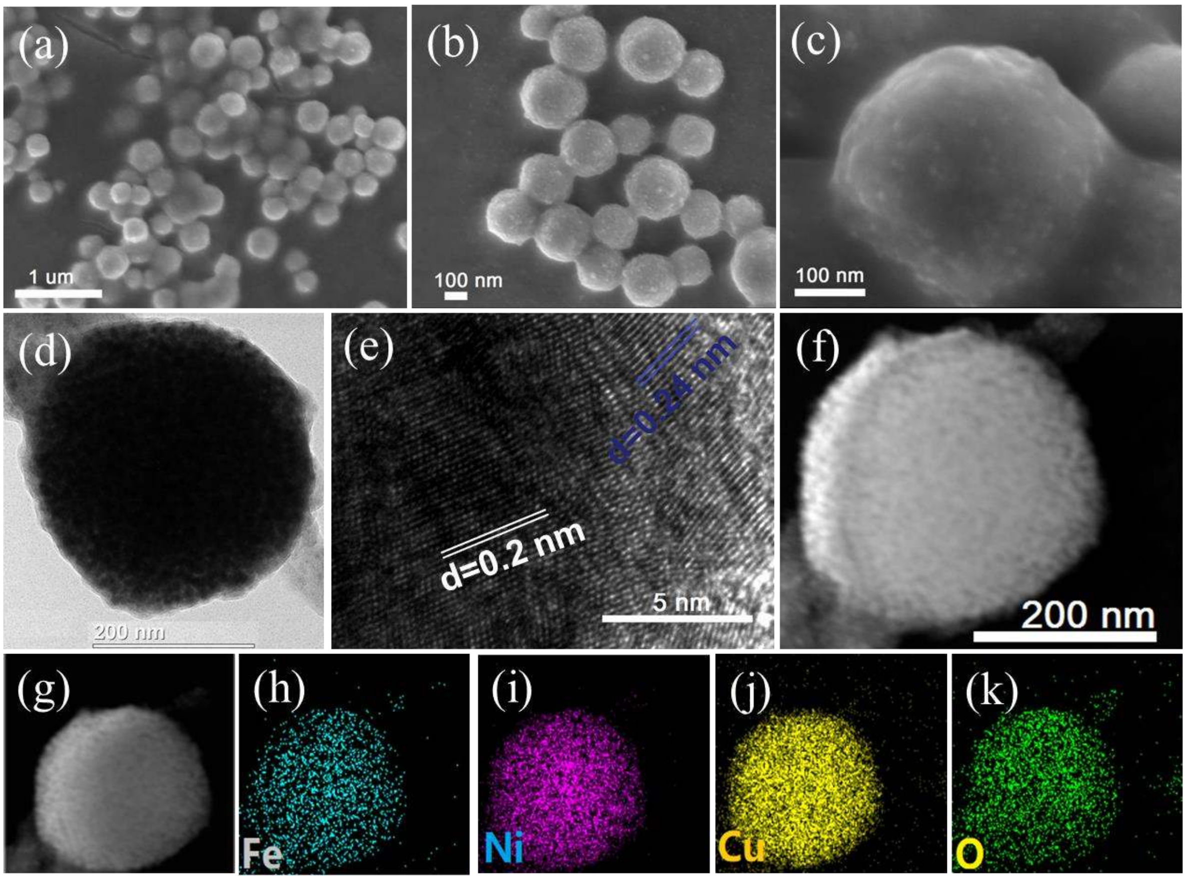

Fig. 2 (a-c) FESEM, (d, f) TEM, (f, g) HAADF-STEM images of NiFeO$_x$@NiCu, and corresponding EELS mapping of (h) iron, (i) nickel, (j) copper and (k) oxygen.

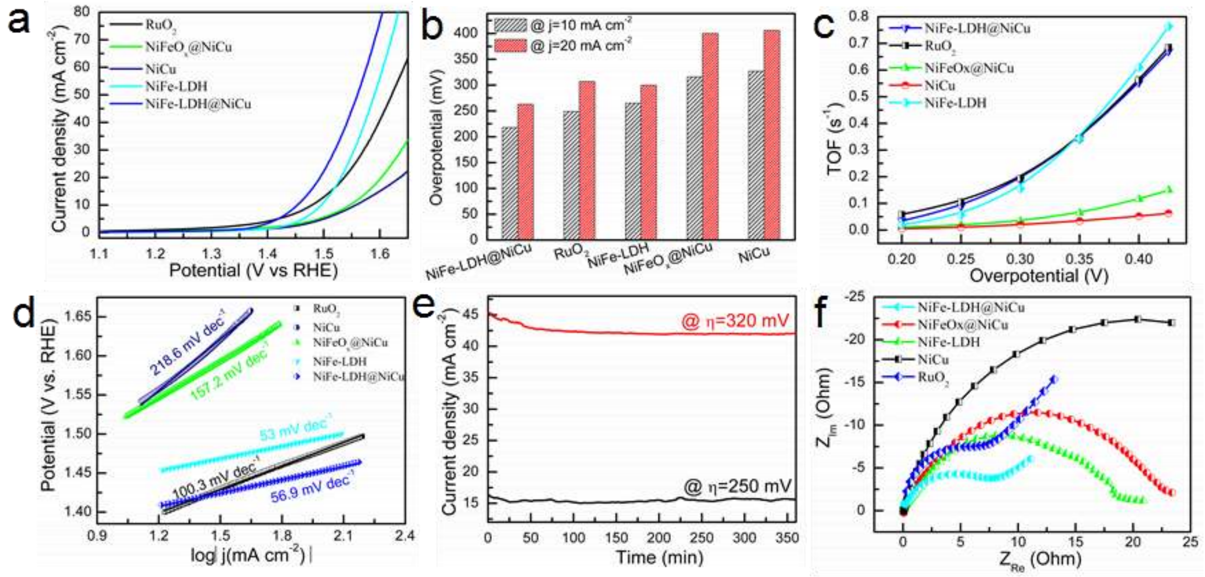

Fig. 3 OER performance of the catalysts in 1 M KOH. (a) Polarization curves recorded with a scan rate of 5 mV s^{-1}, (b) comparison of overpotentials at current densities of 10 and 20 mA cm^{-2}, (c) TOF as a function of overpotential, (d) corresponding Tafel plots, (e) Time dependence of current densities at overpotentials of 250 and 320 mV, and (f) Nyquist plots recorded at an overpotential of 300 mV.

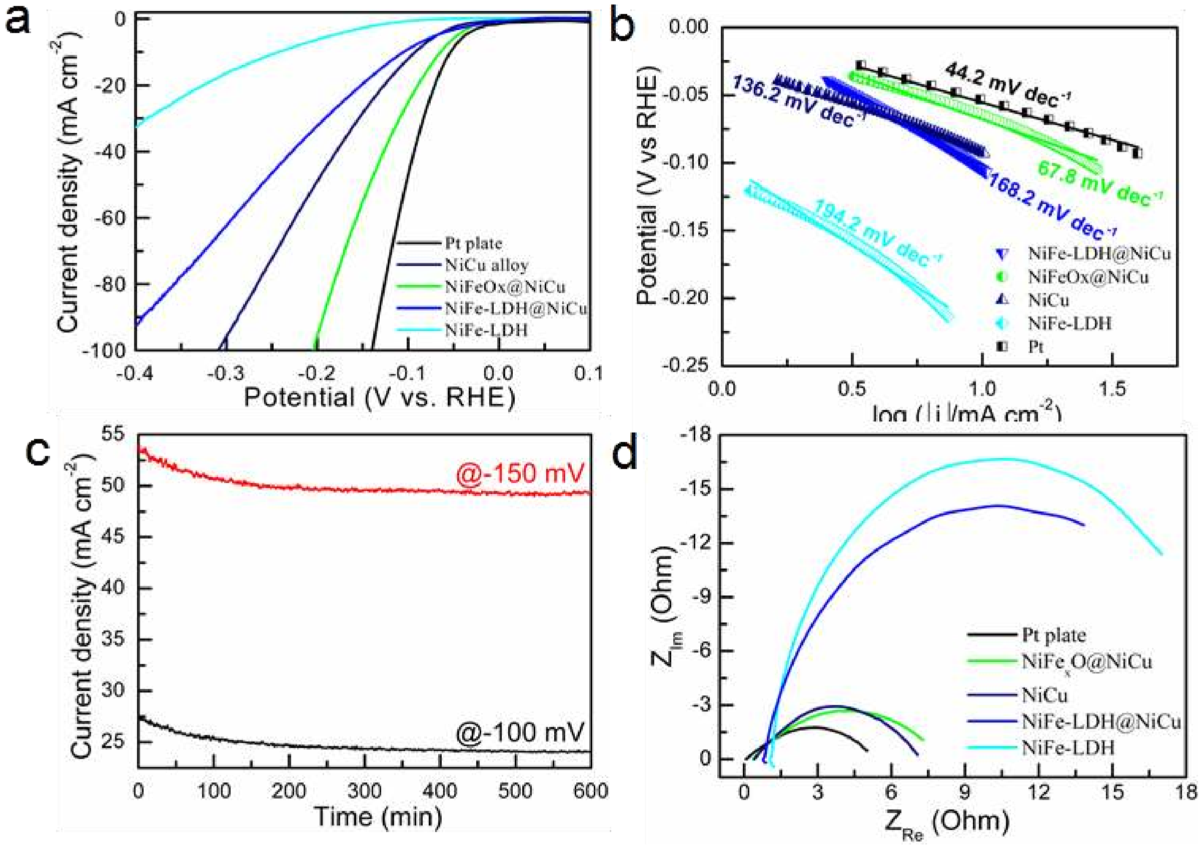

Fig. 4 HER performance of the catalysts in 1 M KOH. (a) HER polarization curves, (b) corresponding Tafel plots, (c) chronoamperometric curves of NiFeOx@NiCu recorded at overpotentials of 100 and 150 mV, and (d) ESI Nyquist plots of the catalysts recorded at an overpotential of 150 mV.

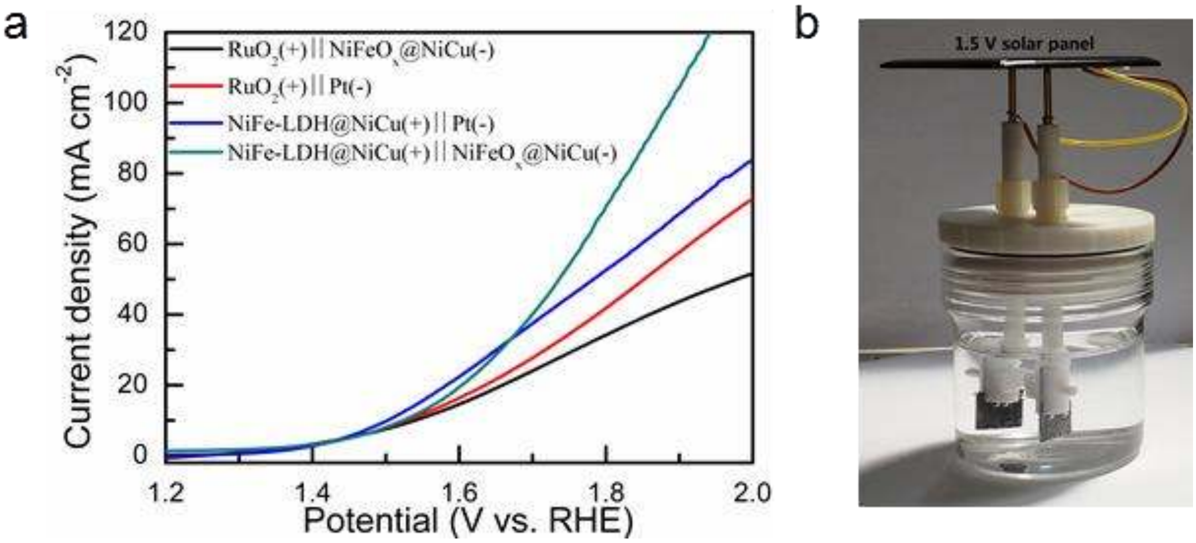

Fig. 5 (a) Linear sweeping voltammetry curves of the catalysts in 1 M KOH for overall water splitting, (b) demonstration of a 1.5 V solar panel powered water splitting using NiFe-LDH@NiCu and $NiFeO_x$@NiCu as anodic and cathodic catalysts, respectively.

The table of contents In this work, we synthesized three-dimensional core-shelled nanoarchitectures, consisting of NiFe-LDH nanosheets/porous NiFe oxides assembled to metallic NiCu alloy, as bifunctional electrocatalysts for overall water splitting. Owing to their unique structures, the as-prepared materials possess exceptional activity for both OER and HER, thus functioning as versatile bifunctional catalysts for overall water splitting. The superior performance was demonstrated by a 1.5 V solar-panel powered electrolyzer, yielding current densities of 10 and 50 mA cm^{-2} at overpotentials of 293 and 506 eV, respectively.

Keyword: water splitting, hydrogen evolution reaction, oxygen evolution reaction, layered double hydroxides and porous Ni-Fe oxides

Yi Shen*, Zixu Wang, Yongfang Zhou, Ziyan Pan, Le Liu, and Jingyu Xi

Exceptional performance of hierarchical Ni-Fe (hydr)oxide@NiCu electrocatalysts for water splitting

ToC figure

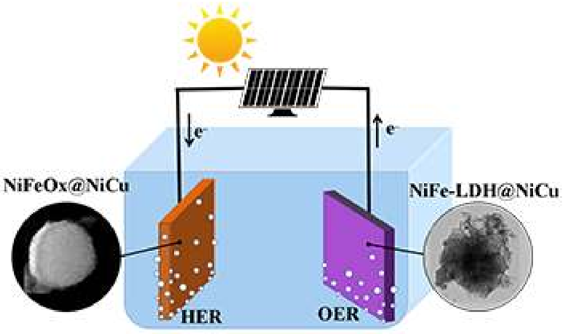

Copyright WILEY-VCH Verlag GmbH & Co. KGaA, 69469 Weinheim, Germany, 2013.

Supporting Information

Exceptional performance of hierarchical Ni-Fe (hydr)oxide@NiCu electrocatalysts for water splitting

Yi Shen*, Zixu Wang, Yongfang Zhou, Ziyan Pan, Le Liu, and Jingyu Xi

*Corresponding author Email: feyshen@scut.edu.cn (Y. S)

Experimental section

Synthesis of catalysts

Synthesis of NiCu alloy NiCu alloy was synthesized via a polyol-assisted reduction process. 7.5 mmol of nickel (II) nitrate hexahydrate and 2.5 mmol of copper (II) nitrate trihydrate were dissolved into 25 mL of ethylene glycol at 80^oC. 150 mL of ethylene glycol was poured into a 250 mL three-necked flask. 1.2 g of sodium hydroxide was introduced into the flask. The flask was heated at 180^oC for 5 min to remove any moisture. Nitrogen gas (purity > 99.99%) was bubbled through the solution to remove any oxygen. Next, the metal precursor solution was transferred into the flask under intense agitation and refluxed at 180^oC for 30 min. Subsequently, the flask was moved to ice water to quench the reaction. The product was collected, thoroughly washed with ethanol, acetone and water to remove impurities, and dried at 80^oC using a vacuum oven overnight.

Synthesis of NiFe-LDH NiFe-LDH was synthesized via a precipitation process. 150 mL of ethylene glycol and 5 mL of de-ionized water were added into a 250 mL beaker. 1.6 g of sodium hydroxide was dissolved into the solution by magnetic stirring. Subsequently, 7.5 mmol of nickel (II) nitrate hexahydrate and 2.5 mmol of iron (III) nitrate nonahydrate were also added. The mixture was heated at 80^oC under magnetic stirring for 30 min. After cooling to room temperature, the product was collected, thoroughly washed with ethanol and water, and dried at 60^oC using a vacuum oven overnight.

Synthesis of NiFe-LDH@NiCu 1.5 mmol of nickel (II) nitrate hexahydrate and 1.0 mmol of copper (II) nitrate trihydrate were reduced by the aforementioned ethylene glycol-assisted reduction method to form stable suspension. When the temperature of the suspension was cooled down to 80^oC, 6.0 mmol of nickel (II) nitrate hexahydrate and 1.5 mmol of iron (III) nitrate nonahydrate were added. The mixture was subjected to intense agitation for 1 h. After cooling to room temperature, the product was collected, thoroughly washed with ethanol and water, and dried at 60°C using a vacuum oven overnight.

Synthesis of NiFeO$_x$@NiCu The synthesis procedure of NiFeO$_x$@NiCu is similar to that of NiFe-LDH@NiCu except that the precipitation reaction was conducted at 120°C for 2 h. To fully dehydrate, the resulting solid was further calcined at 200°C for 2 h using a tube furnace under a nitrogen flow.

Structural Characterization

A field emission scanning electron microscope (FESEM) (JSM-7600F, JEOL) and a transmission electron microscope (FEI Tecnai F30) were used to observe the morphology of the samples. The samples for the TEM tests were prepared by the ultrasonication of the powdered samples in ethanol and the evaporation of one drop of the suspension onto a carbon film supported on a mesh copper grid. An energy dispersive X-ray (EDX) analyzer equipped into the TEM and an axis-ultra X-ray photoelectron spectrometer (Kratos-Axis Ultra System) with monochromatized Al-Kα radiation were used to analyze the elemental composition of the samples. X-ray diffraction (XRD) patterns were obtained by a diffractometer (PW1830, Philips) equipped with Cu-Ka radiation of 1.54 Å. The metal content in the catalyst and the metal ions in the tested electrolyte were determined by inductively coupled plasma atomic emission spectrometry (ICP-AES) (Varian 710-ES) analyses. For atomic force microscopy (AFM) analysis, the powder sample was dispersed into ethanol by ultrasonication and transferred into Si/SiO$_2$ substrates (SiO$_2$ thickness: 300 nm). The image was obtained using Dimension 3100 (Veeco, Santa Barbara, CA) in tapping mode with a Si tip (Veeco; resonant frequency, 320 kHz; spring constant, 42 N m^{-1}) under ambient conditions.

Electrochemical measurements

Electrochemical measurements were performed on an electrochemical station (CHI 760E) connecting with a typical three-electrode cell. A glassy carbon electrode (diameter = 3 mm) was used as a working electrode. The catalyst was transferred into the electrode via a typical casting process as described in the authors' previous work.[1] The cover density of catalyst on the electrode was ca. 80 μg/cm^2. A Hg/HgO electrode and Pt gauze (effective area 1 × 1 cm) were used as reference and counter electrodes, respectively. Linear sweeping voltammetry measurements were conducted in 1 M KOH solution with a scan rate of 5 mV/s. To evaluate the double-layer capacitance cyclic voltammetry measurements were conducted with scan rates of 10, 20, 50, 75 and 100 mV/s in the potential range of 0.4 ~ 0.6 V vs. Hg/HgO. The double-layer capacitance (C_{dl}) was estimated by plotting (J_a-J_c)/2 against scan rate, where J_a and J_c are the anodic and cathodic current densities at 0.5 V vs. Hg/HgO, respectively. Both chronoamperometry and chronopotentiometry tests were conducted to evaluate the durability of the catalyst. Electrochemical impedance spectroscopy (EIS) tests were done from 0.1 Hz to 100 kHz with an amplitude of 10 mV. The turnover frequency (TOF) was calculated by following equation:[2]

$$\mathrm{TOF}=\frac{\mathrm{J}\times\mathrm{A}}{4\times\mathrm{F}\times\mathrm{m}}$$

where J is the current density at a given overpotential, A is the surface area of the electrode, F is the Faradic constant, and m is the number of moles of Ni/Ru on the electrode. All the polarization curves were reported with Ohmic drop correction. All the potentials reported in this work were referenced to reversible hydrogen electrode (RHE) by following equation: E (vs. RHE) = E (vs. Hg/HgO) + 0.098 + 0.059*pH. All the electrochemical measurements were conducted at ambient temperature.

The overall water splitting performance of the catalyst in 1 M KOH was evaluated by a two-electrode configuration. The polarization curves were recorded with a scan rate of 5 mV/s. To demonstrate a solar-energy driven overall water splitting process, a graphite paper (1 × 1 cm) with a catalyst loading of 1 mg/cm^2 was used as an electrode. Two solar panels with voltages of 1.5 and 2.0 V were used to power the water splitting process. The overall water splitting process was conducted outside on a sunny day (T=33±1°C).

Reference

1. Y. Shen, Y. Zhou, D. Wang, X. Wu, J. Li, J. Xi, Adv. Energy Mater. 2018, 8, 1701759
2. F. Song and X. Hu, J. Am. Chem. Soc., 2014, 136, 16481-16484

Table S1 Composition of the catalyst samples determined by ICP-AES (Note: the percentages of oxygen in the samples were determined by the subtraction of total mass of the sample by those of metals).

Sample	Actual atomic composition
RuO_2	Ru (31.4%):O (68.6%)
NiCu	Ni (70.2%):Cu (23.3%):O (6.5%)
NiFe-LDH	Ni (24.2%):Fe (7.6%):O (68.2%)
$NiFeO_x$@NiCu	Ni (45.1%):Cu (5.7):Fe (15.9%):O (33.3%)
NiFe-LDH@NiCu	Ni (34.6%):Cu (4.6):Fe (7.8%):O (53.0%)

Table S2 Surface composition of the catalyst samples determined by XPS.

Sample	Actual atomic composition
NiCu	Ni (52.2%):Cu (18.9%):O (28.9%)
NiFe-LDH	Ni (24.8%):Fe (6.4%):O (68.8%)
$NiFeO_x$@NiCu	Ni (36.3%):Cu (0.7):Fe (18.3%):O (44.7%)
NiFe-LDH@NiCu	Ni (30.2%):Cu (0.7):Fe (12.9%):O (56.2%)

Table S3 Comparison of the OER performance of the transitional metal-based (hydr)oxide electrocatalysts.

Electrocatalyst	Overpotential (mV) (*j* =10 mA cm^{-2})	Loading (mg cm^{-2})	Electrolyte	Reference
NiFe-LDH@NiCu	218	0.4	1.0 M KOH	This work
NiFeOx@NiCu	316			
Cu@NiFe LDH	199	2.2	1.0 M KOH	*Energy Environ. Sci.* **2017**, 10, 1820-1827
NiFe LHD-NS@DG	210	0.28	1.0 M KOH	*Adv. Mater.* **2017**, 29, 1700017
NiCo hydroxide	460	N.A.	0.1 M KOH	*Adv. Funct. Mater.* **2014,** 24, 4698-4705
Ni-Fe LDH	308	0.20	0.1 M KOH	*J. Am. Chem. Soc.* **2013,** 135, 8452-8455
MWCNTs/$Ni(OH)_2$	474	0.28	0.1 M KOH	*J. Mater. Chem. A* **2014,** 2, 11799-11806
$Ni(OH)_2$	595	0.28	0.1 M KOH	*J. Mater. Chem. A* **2014,** 2, 11799-11806
NiCoFe LDH/CFC	239	0.40	1.0 M KOH	*ACS Energy Lett.* **2016**, *1, 445-453*
$Ni(OH)_2$	331	0.20	0.1 M KOH	*J. Am. Chem. Soc.* **2014,** 136, 7077-7084
Co–Fe–O/rGO	340	0.10	1.0 M KOH	*ChemSusChem* **2015**, 8, 659-664
NiCo LDH	367	0.17	1.0 M KOH	*Nano Lett.* **2015**, 15, 1421-1427
Ni–Fe LDH/CNT	247	0.20	1.0 M KOH	*J. Am. Chem. Soc.*, **2013**, 135, 8452–8455
CoMn-LDH/CNT	335	0.20	1.0 M KOH	*ChemElectroChem*, **2016,** 3, 906-912
NiFe LDH/RGO	245	1.0	1.0 M KOH	*J. Power. Sources.* **2015**, 294, 437-443
CoFe LDH	325	0.20	0.1 M KOH	*Adv. Mater. Inter*, **2016**, 3, 1500782
CoMn LDH	324	0.142	1.0 M KOH	*J. Am. Chem. Soc.*, **2014**, 136, 16481-16484
Exfoliated NiFe LDH	302	0.07	1.0 M KOH	*Nat. Commun.* **2014**, 5, 9
O-NiCoFe-LDH	340	1.0	0.1 M KOH	*Adv. Energy Mater.***2015**, *5, 1500245*
NiCoFe LDH	239	0.3	0.1 M KOH	*J. Mater. Chem. A,* **2016**,*4, 7245*

Table S4 Comparison of the HER performance of the electrocatalysts in 1 M KOH.

Electrocatalyst	Overpotential (mV) (*j* =10 mAcm^{-2})	Loading (mg cm^{-2})	Reference
NiCoFe LTHs/CFC	200	0.4	*ACS Energy Lett.* **2016**, 1, 445-453
Ni nanowires	350	1.0	*ACS Catal.* **2013,** 3, 166-169
Bulk MoB	225	0.5	*Angew. Chem. Int. Ed.* **2012,** 124, 12875-12878
Bulk Mo$_2$C	195	0.8	*Angew. Chem. Int. Ed.* **2012,** 124 (51), 12875-12878.
Porous NiSe$_2$ nanosheets	184	0.46	*Chem. Mater.* **2015,** 27, 5702-5711.
Ni$_5$P4 Films	150	N.A.	*Angew. Chem. Int. Ed.* **2015**, 127, 12538-12542
CoP/CC	209	0.92	*J. Am. Chem. Soc.* **2014,** 136, 7587-7590.
Ni$_2$P	220	5.0	*Energy Environ. Sci.* **2015,** 8, 2347-2351.
NiFe LDHs	219	N.A.	*Science* **2014,** 345, 1593-1596.
MoC$_X$	151	0.8	*Nat Commun* **2015,** 6, 6512.
Co NPs@N-CNTs	370	0.28	*Angew. Chem. Int. Ed.***2014,** 126, 4372-4376.
NiFe-LDH-NS@DG	300	0.28	*Adv. Mater.* **2017**, 29, 1700017
	115	2.0	
Cu@NiFe LDH	116	2.2	*Energy Environ. Sci.* **2017**, 10, 1820-1827
NiO/Ni-CNT	< 100	0.28	*Nat. Commun.* **2014**, *5, 4695*
NiFe-LDH@NiCu	112	0.4	This work
NiFeOx@NiCu	66		

Table S5 Comparison of overall-water-splitting performance of the electrocatalysts in 1M KOH.

Electrocatalyst	Current density (mA cm^{-2})	Potential (V)	Loading (mg cm^{-2})	Reference
NiFeOx@NiCu (-)||NiFe-LDH@NiCu (+)	10	1.52	1.0	This work
	50	1.73		
Pt (-)||NiFe-LDH@NiCu (+)	10	1.50	2.0	
	50	1.78		
NiFeOx@NiCu (-)||RuO_2 (+)	10	1.54	1.0	
	50	1.98		
Pt (-)||RuO_2 (+)	10	1.53	1.0	
	50	1.85		
NiFe-LDH-NS@DG	20	1.50	2.0	*Adv. Mater.* **2017**, 29, 1700017
NiCoFe LTHs/CFC	10	1.55	0.4	*ACS Energy Lett.* **2016**, 1, 445-453
Cu@NiFe LDH	10	1.54	2.2	*Energy Environ. Sci.* **2017**, 10, 1820-1827
Ni_5P_4 films	10	1.70	N.A.	*Angew. Chem. Int. Ed.* **2015**, 127, 12538-12542
NiSe Nanowires/Ni foam	10	1.63	2.8	*Angew. Chem. Int. Ed.* **2015**, 127, 9483-9487
NiFe LDHs/NF	10	1.70	N.A.	*Science*, **2014**, 345, 1593-1596
$Ni(OH)_2$/NF	10	1.82	N.A.	*Science*, **2014**, 345, 1593-1596
NiMo HNRs	10	1.64	0.68	*J. Mater. Chem. A* **2015**, 3, 20056-20059
RuO_2/TiMIIPt/C/TiM	10	1.57	0.68	*J. Mater. Chem. A 2015*, 3, 20056-20059
Ni_2P	10	1.63	0.14	*Energy Environ. Sci.* **2015**, 8, 2347-2351
CoP films	10	1.63	1.0	*Angew. Chem. Int. Ed.***2015**, 54, 6251-6254.

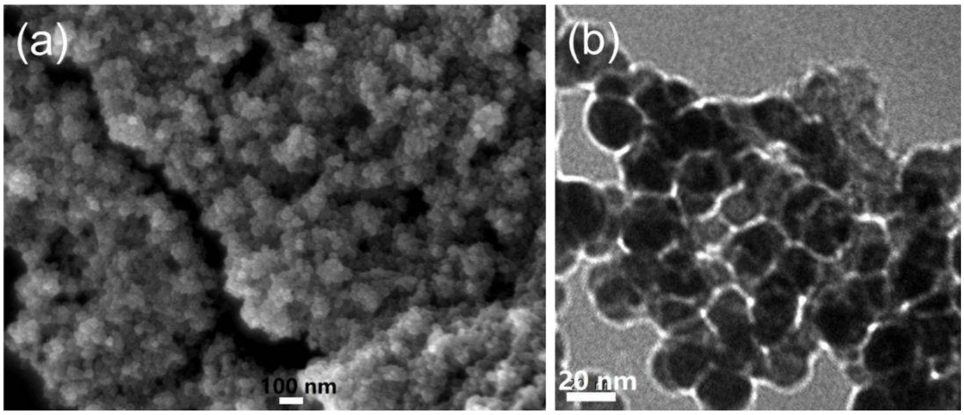

Figure S1 (a) FESEM and (b) TEM images of NiCu alloy nanoparticles.

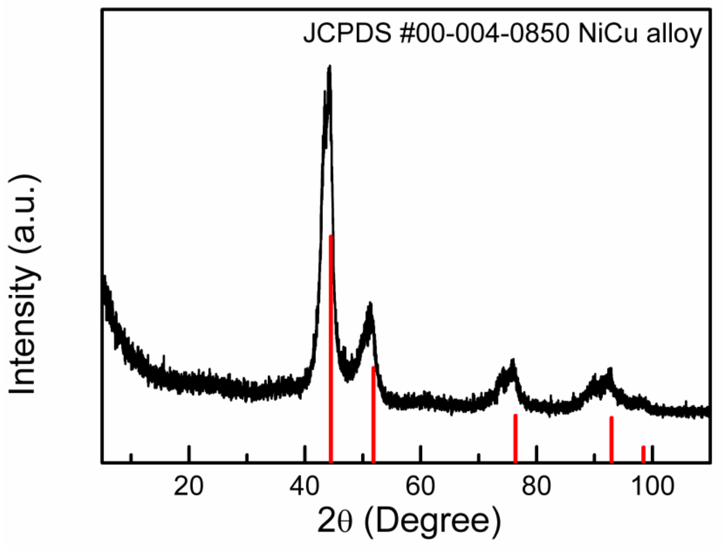

Figure S2 XRD pattern of NiCu alloy nanoparticles.

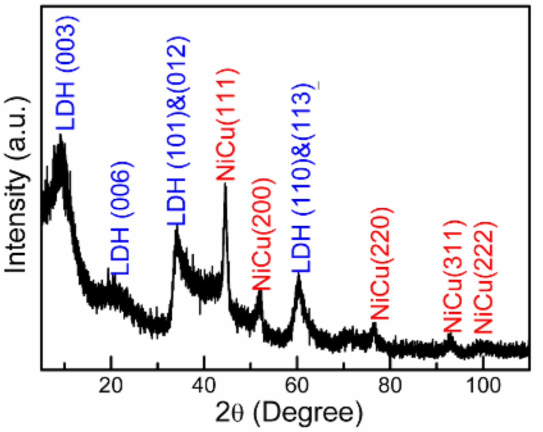

Figure S3 XRD pattern of NiFe-LDH@NiCu.

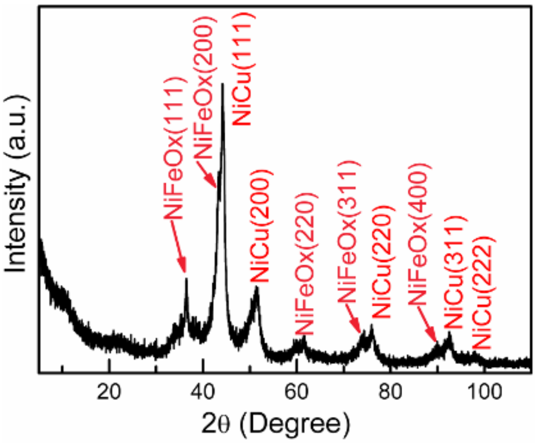

Figure S4 XRD pattern of $NiFeO_x$@NiCu.

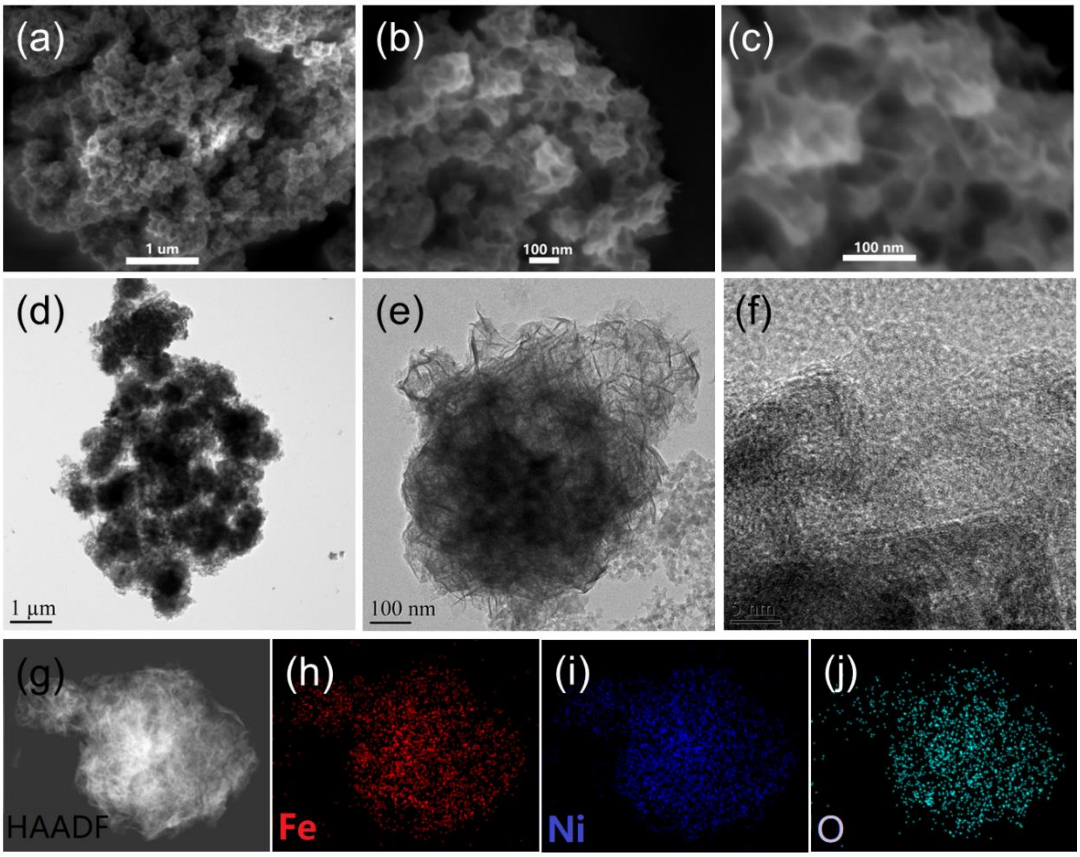

Figure S5 (a-c) FESEM, (d-f) TEM, (g) High-angle annular dark field scanning transmission electron microscopy images of NiFe-LDH, and corresponding EELS mapping of (h) Fe, (i) Ni and (j) oxygen.

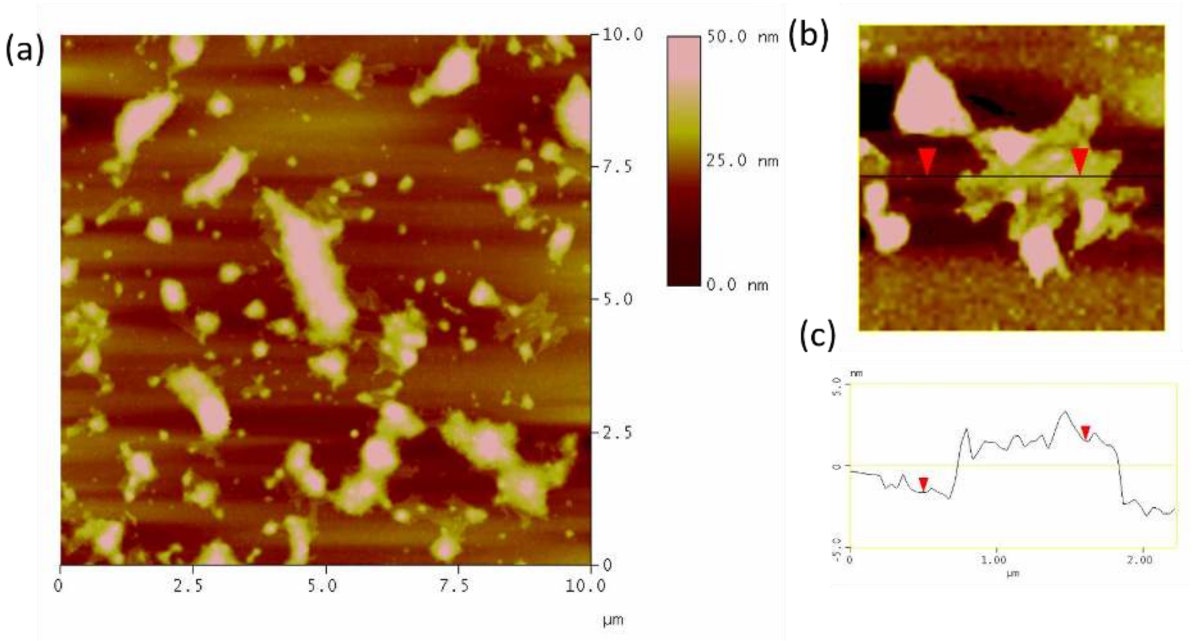

Figure S6 (a, b) AFM images of the NiFe-LDH nanosheets and (c) the corresponding height profile of the line scan shown in (b)

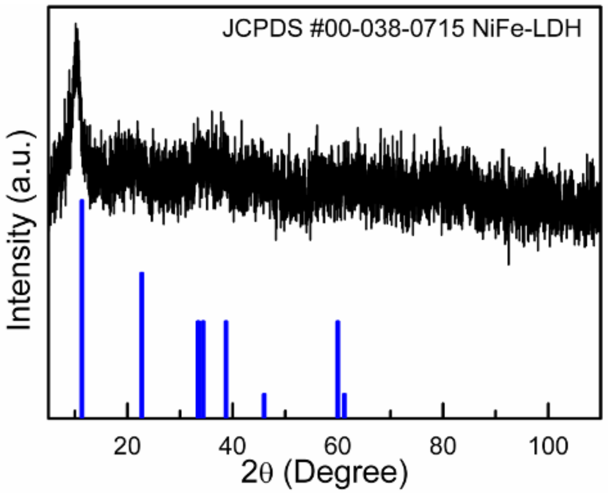

Figure S7 XRD pattern of NiFe-LDH.

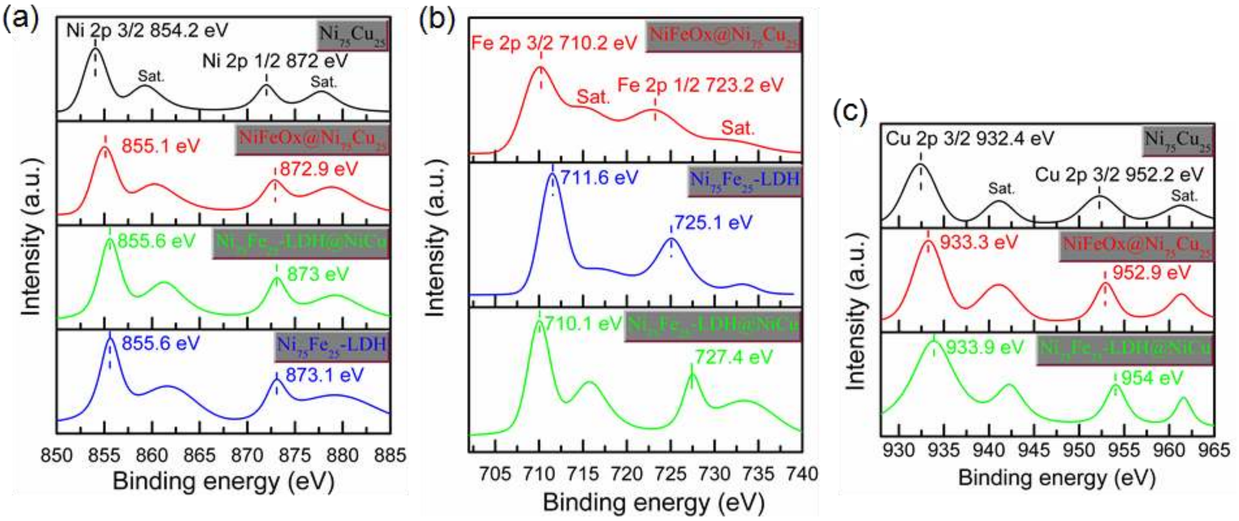

Figure S8 XPS spectra of (a) Ni 2p, (b) Fe 2p and (c) Cu 2p of the samples.

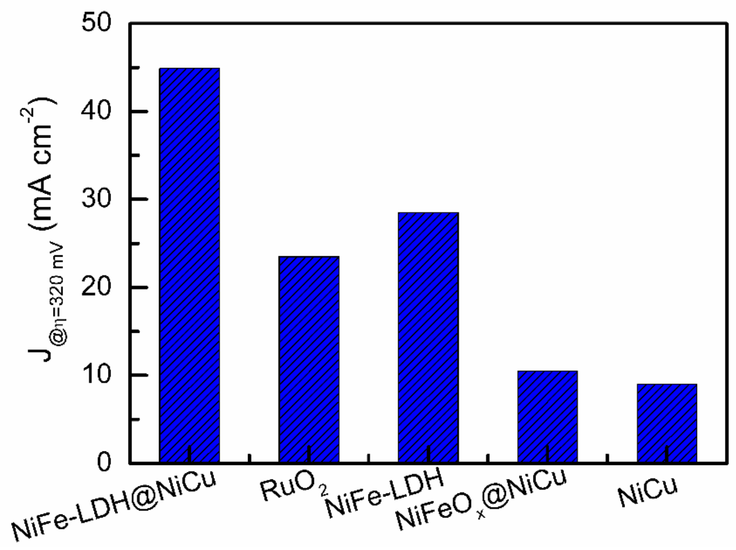

Figure S9 Comparison of OER current densities of the catalysts at an overpotential of 320 mV.

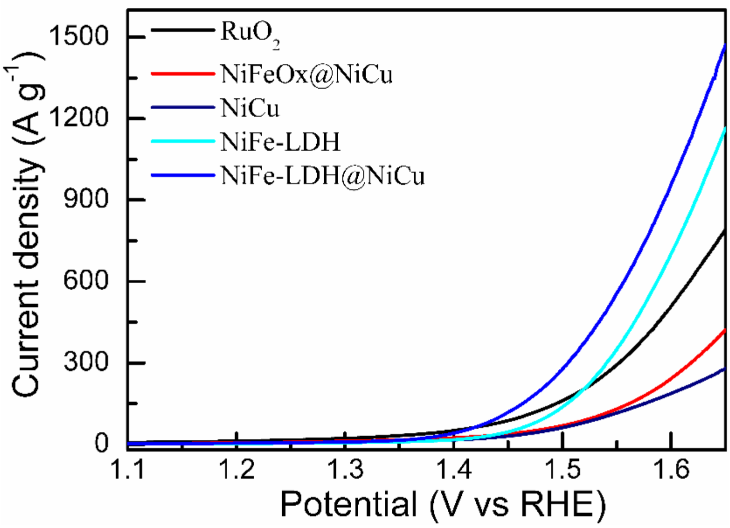

Figure S10 Mass-normalized current densities of the catalysts.

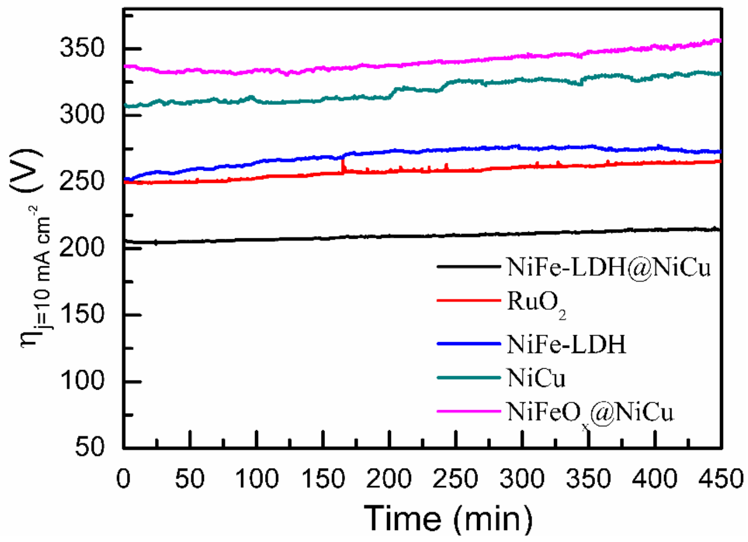

Figure S11 Chronopotentiometry curves of the catalysts at a constant current density of 10 mA cm^{-2}.

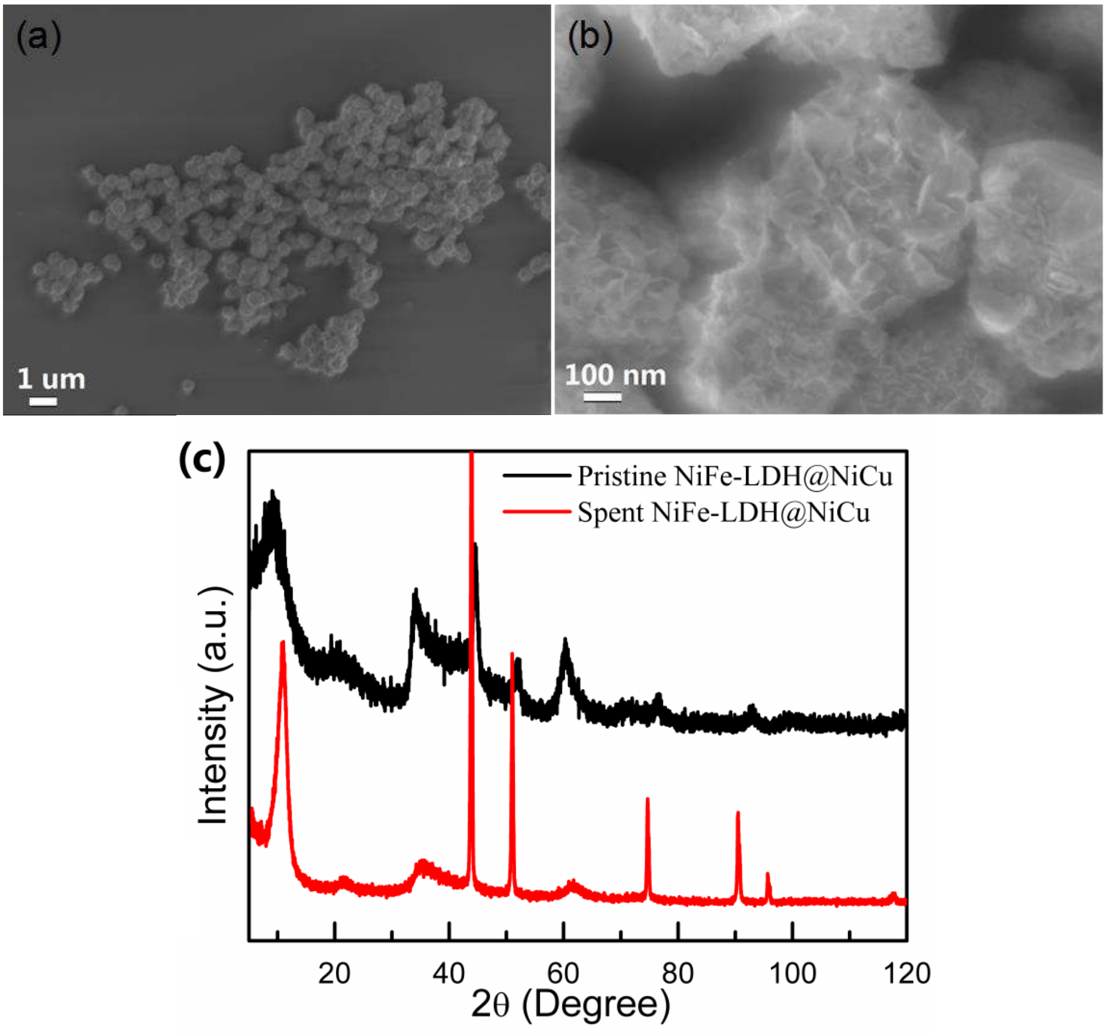

Figure S12 (a, b) FESEM images of the spent NiFe-LDH@NiCu catalyst after the chronoamperometric measurement, and (c) XRD patterns of the pristine and spent NiFe-LDH@NiCu catalysts.

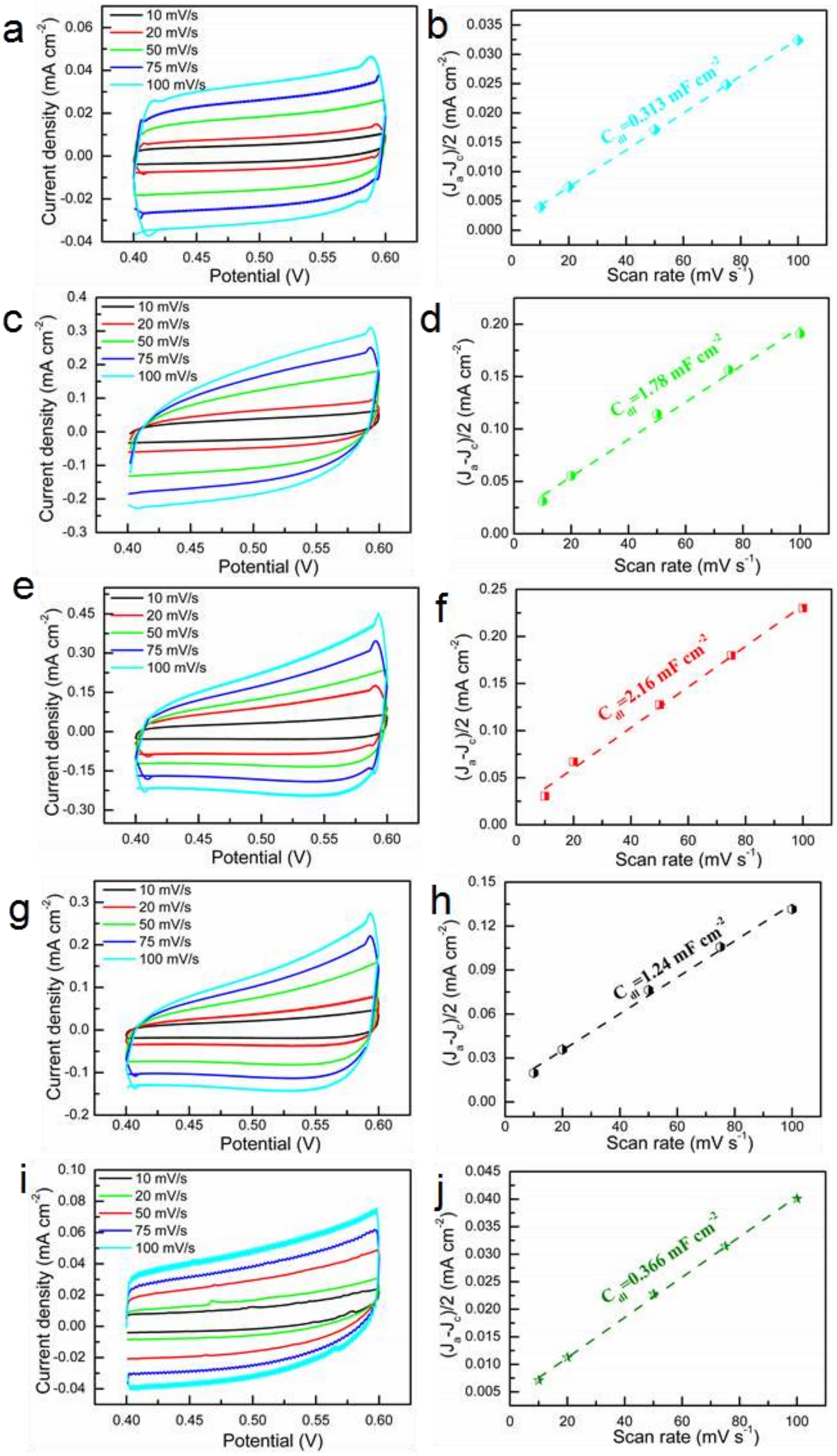

Figure S13 (a, c, e, g and i) CVs recorded at a potential range of 0.4 to 0.6 V with varying scan rates, and (b, d, f, h and j) corresponding half charging current density differences $(J_a-J_c)/2$ plotted against scan rate. (a, b), (c, d), (e, f), (g, h) and (i, j) are NiCu, NiFe-LDH@NiCu, NiFe-LDH, NiFeO$_x$@NiCu and RuO$_2$, respectively.

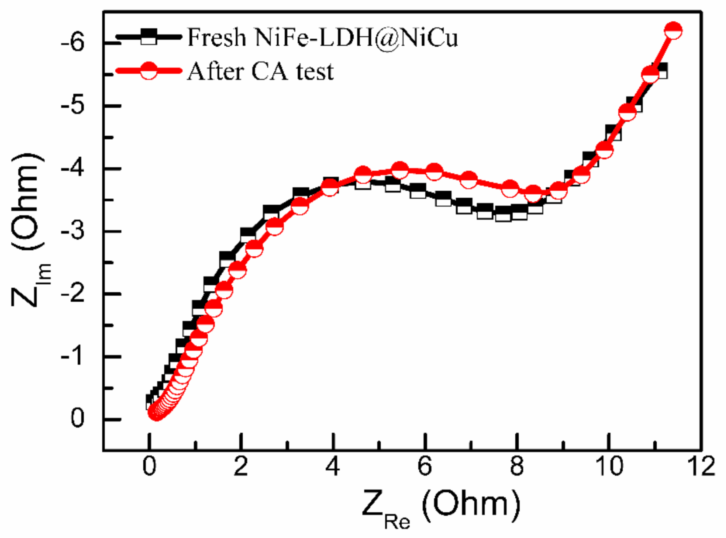

Figure S14 Electrochemical impedance spectroscopy Nyquist plots of NiFe-LDH@NiCu catalyst before and after chronoamperometric measurements.

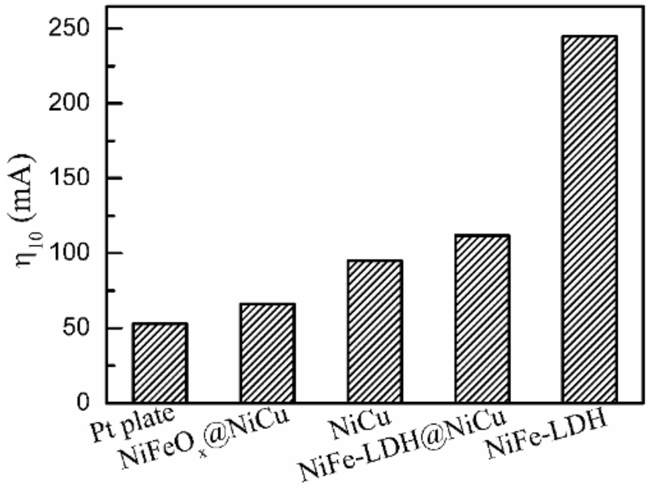

Figure S15 Comparison of overpotentials of the catalysts at a constant HER current density of 10 mA cm^{-2}.

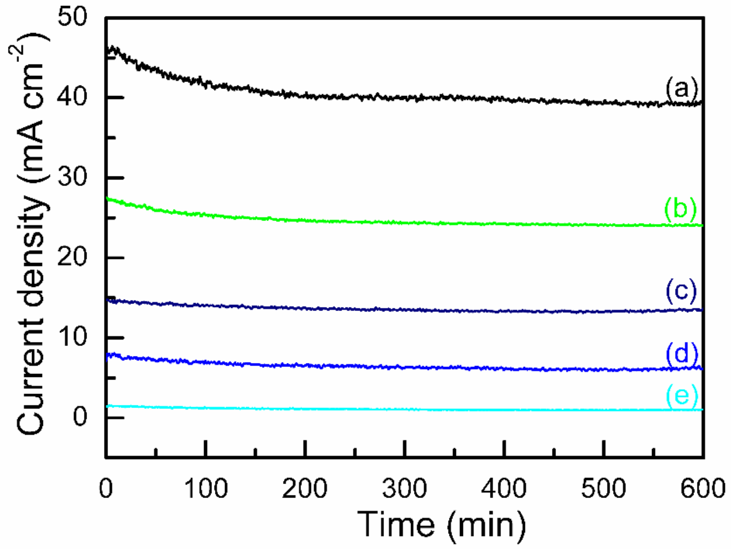

Figure S16 Chronoamperometric curves of (a) Pt, (b) NiFeO$_x$@NiCu, (c) NiCu, (d) NiFe-LDH@NiCu, and (e) NiFe-LDH recorded at a constant overpotential of 100 mV.

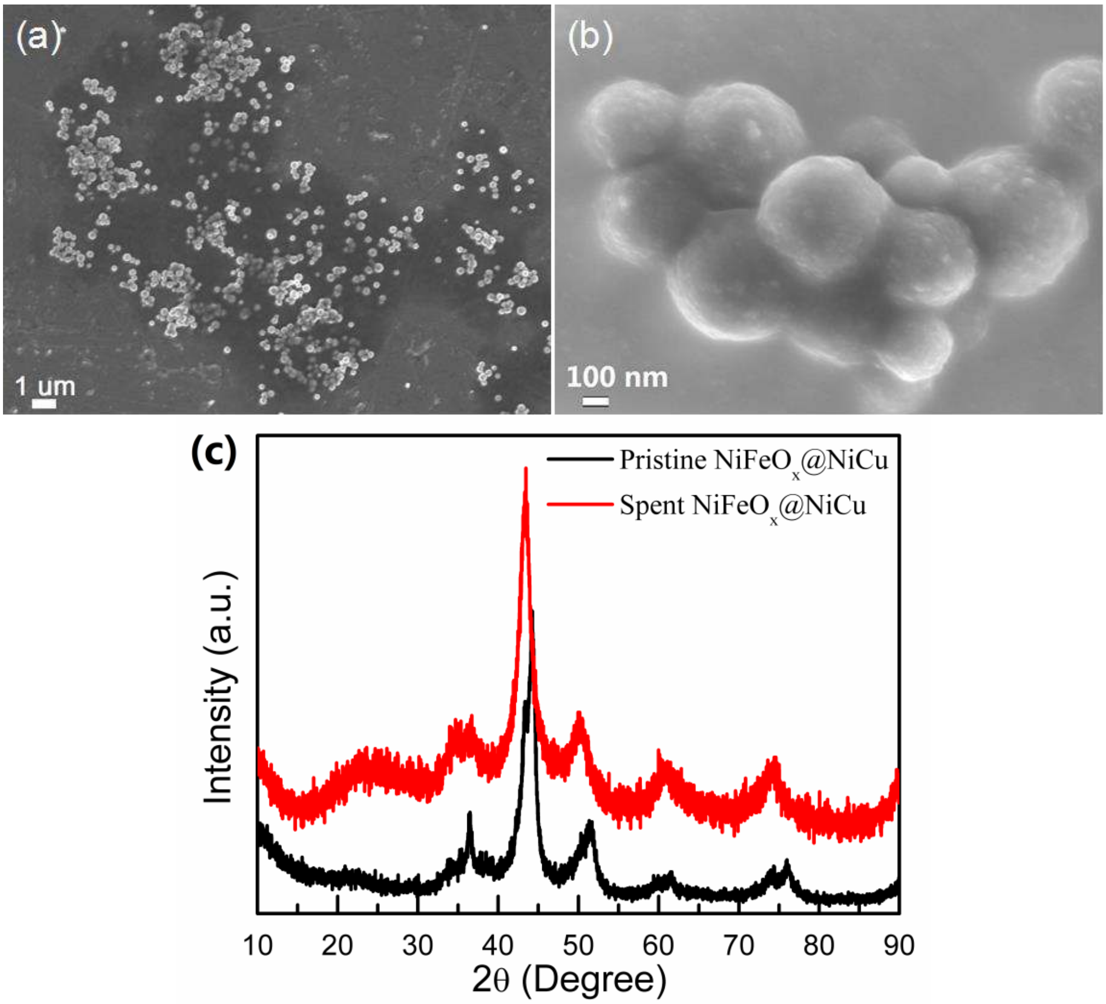

Figure S17 (a, b) FESEM images of the spent NiFeO$_x$@NiCu after the chronoamperometric measurement, and (c) XRD patterns of the pristine and spent NiFeO$_x$@NiCu catalysts.

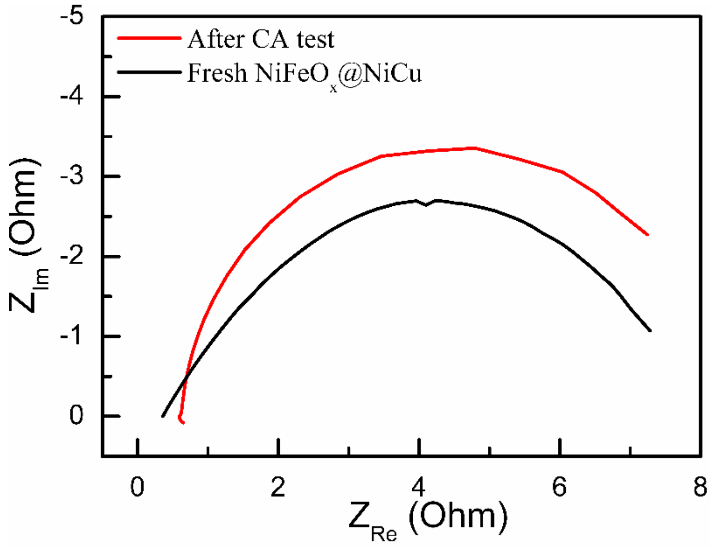

Figure S18 Electrochemical impedance spectroscopy Nyquist plots of NiFeO$_x$@NiCu catalyst before and after chronoamperometric measurements.

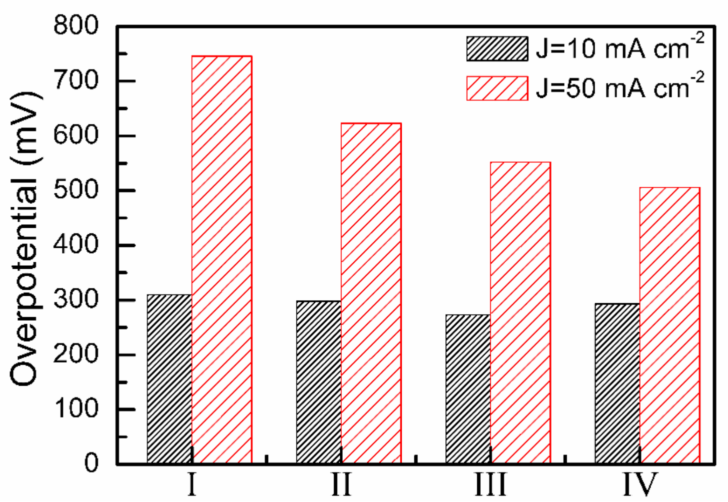

Figure S19 Comparison of the required voltages for overall water splitting at current densities of 10 and 50 mA cm^{-2}. (I) RuO_2(+)||$NiFeO_x$@NiCu(-), (II) RuO_2(+)||Pt(-), (III) NiFe-LDH@NiCu(+)||Pt(-), and (IV) NiFe-LDH@NiCu(+)||$NiFeO_x$@NiCu(-).